Department of Physics
High Energy Physics Research Group
April 2024

Development of an Ion-Acoustic Dose-Deposition Mapping System for LhARA

Ionacoustics Report

Abstract

LhARA, the Laser-hybrid Accelerator for Radiobiological Applications, is designed to advance radiotherapy and radiation biology research using proton and ion beams. Such beams deposit most of their energy in a small volume of tissue at the end of the particles' range. For this reason, a real-time dose-deposition mapping system is being developed to minimize radiation uncertainties. A proof-of-principle experiment, to be performed at the LION beamline in Munich, has been designed and simulated to evaluate the use of ionacoustic imaging in providing the dose-deposition profile.

Contents

1 Dosimetry

Dosimetry refers to the measurement of absorbed dose and ensures that the appropriate amount of radiation is delivered accurately and safely to the patients [1]. Various methods have been explored for assessing dosimetry during ion-beam irradiation.

1.1 Ion-Acoustic Imaging

Ion-acoustic imaging is a non-invasive modality that uses acoustic pulses induced by the proton or ion energy depositions [2]. When the beam propagates through a medium it interacts with it via Coulomb scatterings and transfers some of its kinetic energy to the atoms in the form of heat. This results in thermoelastic expansion and local pressure increase which results in the emission of an acoustic (pressure) wave. Ultrasound transducers can be used to detect them and the received signals can be processed and used to form an image of the pressure distribution. Due to the extremely high speed of acoustic waves in media, real-time imaging can be performed in a few seconds.

1.2 Scintillators

Scintillators are materials commonly used in radiation detection measurements due to their property of emitting light when exposed to ionizing radiation [3]. When radiation interacts with a scintillator, it imparts energy to the atoms within the material, exciting them to higher energy states. Subsequently, as these excited atoms return to their ground state, they release the excess energy in the form of photons. These emitted photons can be detected and measured to quantify the intensity and nature of the incident radiation. Scintillators come in many forms such as solids or liquids, including organic and inorganic varieties.

1.3 Dose Mapping

For LhARA, an on-the-fly, non-invasive, dose-deposition mapping system needs to be developed that would provide a quantitative 4D dose deposition profile and Bragg peak localization. Such a system will minimize dose delivery uncertainty and enable a more reliable, real-time pulse-to-pulse adaptive treatment planning.

The development of this diagnostics system is based on ion-acoustic imaging. To confirm the fundamental ability of ion-acoustics to provide the beam profile within the required

time frame for LhARA, a series of simulations have been developed using Python [4], BDSIM [5], Geant4 [6] and k-Wave [7]. Figure 1 illustrates the simulation pipeline.

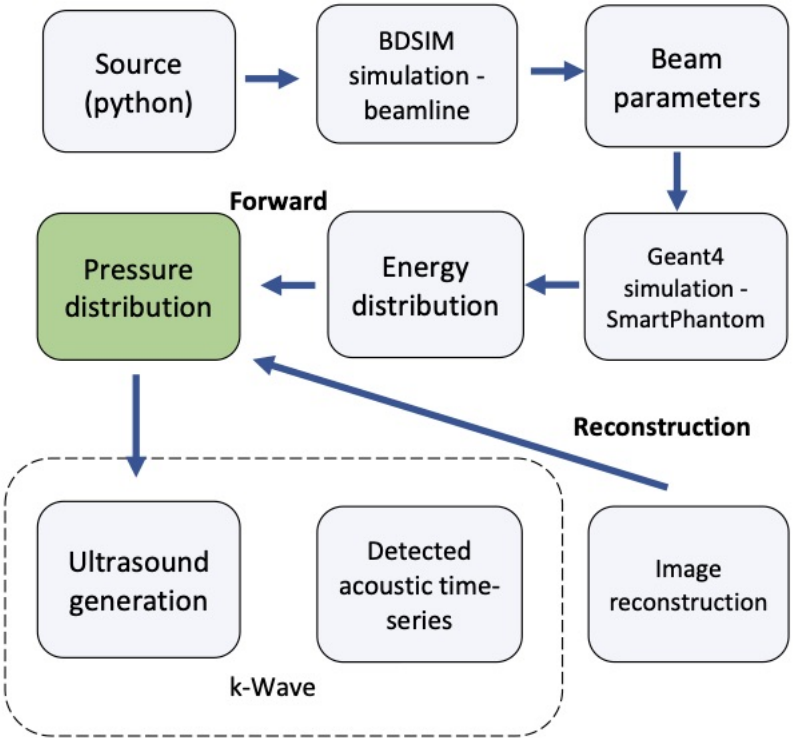

Figure 1. An outline of the LhARA ionacoustics proof-of-principle simulation pipeline.

For calibration, the acoustic measurement should correlated to a known "standard". This can be done by using a liquid scintillator and scintillating fibres of known photon yield and exposing them simultaneously to a known beam.

2 LION Beam Line

The LhARA ionacoustics proof-of-principle activity is planned to be performed at the laser-driven ion (LION) accelerator at the Centre for Advanced Laser Applications (CALA) in Munich, Germany [8]. The proton beam is accelerated via the TNSA mechanism, at a repetition rate of 10 Hz. This acceleration approach and repetition rate are similar to LhARA, making the facility an ideal location for the experiment.

2.1 Source

To parametrize the energy distribution of the particles at the source, the analytical approximation defined in Equation 2.1 [9] has been used, where N is the number of ions per unit solid angle and ϵ is the ion kinetic energy. All the variables present, with associated units, are shown in Table 1, and are based on the laser and foil target used at the LION beamline to accelerate a proton bunch.

$$\frac{dN}{d\varepsilon} = \frac{n_{e0} c_s t_{laser} S_{sheath}}{\sqrt{2\varepsilon T_e}} exp(-\sqrt{\frac{2\varepsilon}{T_e}}) \tag{2.1}$$

The ions which are accelerated by this mechanism have a cut-off energy, ϵ_{max}, which can be calculated using Equation 2.2, where $\epsilon_{i,\infty}$ is the maximum energy for infinite acceleration and X is obtained by solving 2.3 [10]. Performing a third order Taylor expansion, X can be calculated using Equation 2.4.

$$\varepsilon_{max} = X^2 \varepsilon_{i,\infty} \tag{2.2}$$

$$\frac{t_{laser}}{t_0} = X(1 + \frac{1}{2}\frac{1}{1-X^2}) + \frac{1}{4} ln \frac{1+X}{1-X} \tag{2.3}$$

$$X = tanh \frac{t_{laser}}{t_0} \tag{2.4}$$

Parameter	Definition	Value	Unit
N	Ion number	-	-
ε	Ion energy	-	J
n_{e0}	Hot electron density	$\frac{N_E}{ct_{laser}S_{sheath}}$	pp/m^3
N_e	Accelerated electron number	$\frac{fE_{laser}}{T_e}$	-
E_{laser}	Laser energy	70	J
f	Energy conversion efficiency	$1.2 \times 10^{-15} I^{0.75}$, max=0.5	-
I	Laser intensity	4×10^{20}	W/cm^2
T_e	Hot electron temperature	$m_e c^2[\sqrt{1 + \frac{I\lambda^2}{1.37\times10^{18}}} - 1]$	J
m_e	Electron mass	9.11×10^{-31}	Kg

c	Speed of light	3×10^8	m/s
λ	Laser wavelength	0.8	μm
t_{laser}	Laser pulse duration	28×10^{-15}	s
B	Radius of electron bunch	$B = r_0 + dtan(\theta)$	m
S_{sheath}	Electron acceleration area	πB^2	m^2
r_0	Laser spot radius	$\sqrt{\frac{P_{laser}}{I\pi}}$, I in W/m^2	m
d	Target thickness	$400 - 600 \times 10^{-9}$	m
θ	Electron half angle divergence	0.436	rad
P_{laser}	Laser power	2.5×10^{15}, $P_{laser} = \frac{E_{laser}}{t_{laser}}$	W
c_s	Ion-acoustic velocity	$(\frac{Zk_BT_e}{m_i})^{\frac{1}{2}}$	m/s
Z	Ion charge number	1	-
k_B	Boltzmann constant	1.380649×10^{-23}	$m^2kgs^{-2}K^{-1}$
m_i	Proton mass	1.67×10^{-27}	Kg
P_R	Relativistic power unit	$\frac{m_ec^2}{r_e} = 8.71 \times 10^9$	W
r_e	Electron radius	2.82×10^{-15}	m
$\varepsilon_{i,\infty}$	Maximum ion energy	$2Zm_ec^2\sqrt{\frac{fP_{laser}}{P_R}}$	MeV
t_0	Ballistic time	$\frac{B}{v(\infty)}$	s
$v(\infty)$	Ballistic velocity	$\sqrt{\frac{2\varepsilon_{i,\infty}}{m_i}}$	m/s

Table 1: Parameters present in the TNSA analytical equations 2.1 and 2.4 [9] [10].

The angular distribution of the particles at the source has been simulated as Gaussian. Figure 2 shows the parametrized energy and angular distribution of the particles at the LION beamline source.

2.2 Accelerator Configuration

The LION beamline configuration to focus a 20 MeV proton beam is shown in Figure 3. To capture and focus the beam, a set of quadrupole magnets is used. Due to the ability of quadrupoles to focus in one plane and decofus in the other, a combination of two quadrupoles placed perpendicular to each other results in the net focusing of the beam. By varying their location, different energies can be focused on the target.

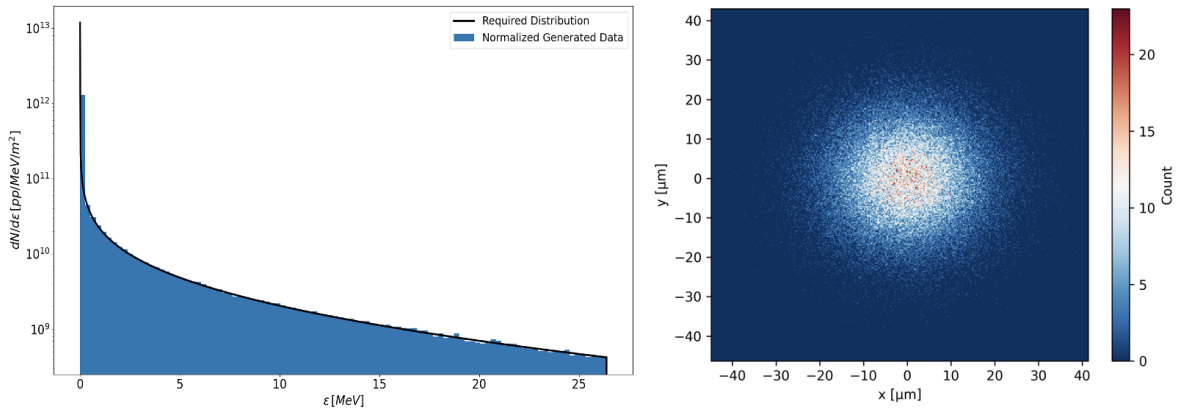

Figure 2. Parametrized energy (left) and angular distribution (right) of the particles at the source of the LION beamline.

An elliptical collimator is placed in front of the first magnet to provide radiation protection and to determine the initial shape of the beam. In addition, a Kapton and an aluminium foil at the exit window stop any electromagnetic radiation that would contribute to noise. Such a combination of the foils allows protons up to 2.1 MeV to be stopped. Moreover, a collimator is placed after the exit window to decrease the phase space of the particles that enter the phantom.

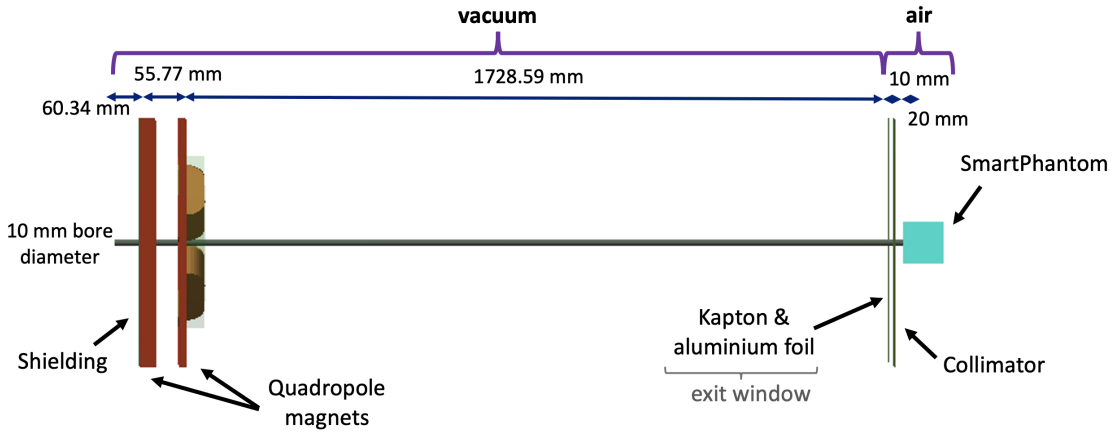

Figure 3. Schematic diagram of the BDSIM simulation of LION beamline, to focus a 20 MeV proton beam.

The energy spectrum and shape of the beam focused onto the phantom are shown in Figure 4. From this figure, it can seen that most of the particles have an energy of $\sim$ 20 MeV, with a standard deviation of 0.65. Furthermore, the cross-sectional area of the beam

can be described as a 'cross' shape, with a full width at half maximum of 0.77 mm along the x-axis and 0.39 mm along the y-axis. All these values agree with experimental results.

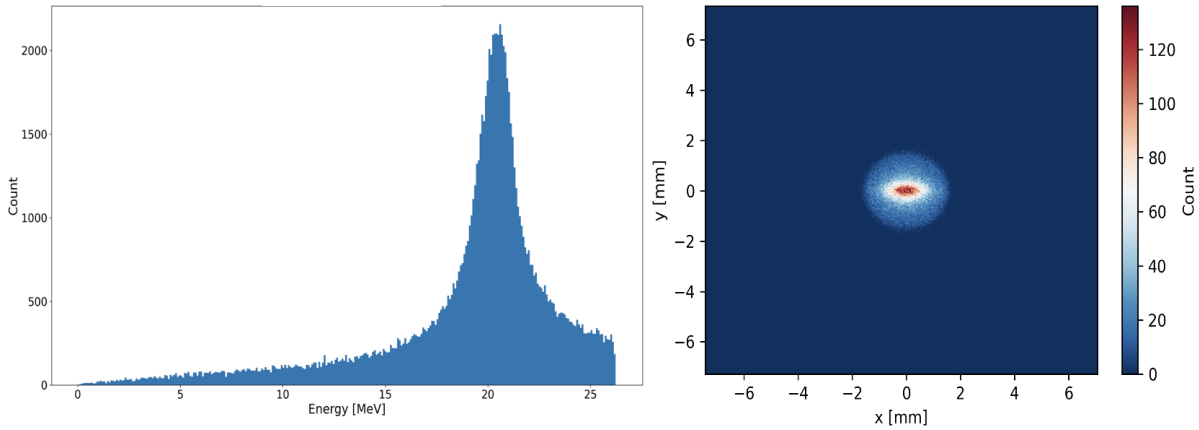

Figure 4. Simulated energy spectrum (left) and spot size (right) of the particles that arrive at the end of the LION beamline.

3 SmartPhantom

The SmartPhantom is proposed to be composed of a chamber filled with a de-ionised water-based scintillating solution. The energy depositions caused by the passage of the ion beam can be retrieved by detecting the induced acoustic signals and by detecting the scintillation light caused by the energy depositions. These data can then be calibrated to infer the dose distribution.

3.1 Design

The Geant4 simulation of the SmartPhantom is shown in Figure 5. The elongated entrance window ensures that the Bragg peak of a 20 MeV proton beam occurs at the centre. This can aid the reconstructions, as cameras and transducers can be placed equidistant from it. The kapton foil acts as an air-water boundary, without distorting the beam.

3.2 Pressure Profile

The time-varying energy output from Geant4 was used as the source acoustic input into k-Wave, to simulate the ion energy transfer to the medium, the generation of the acoustic waves and their propagation in the three-dimensional space until detection. Figure 6 shows

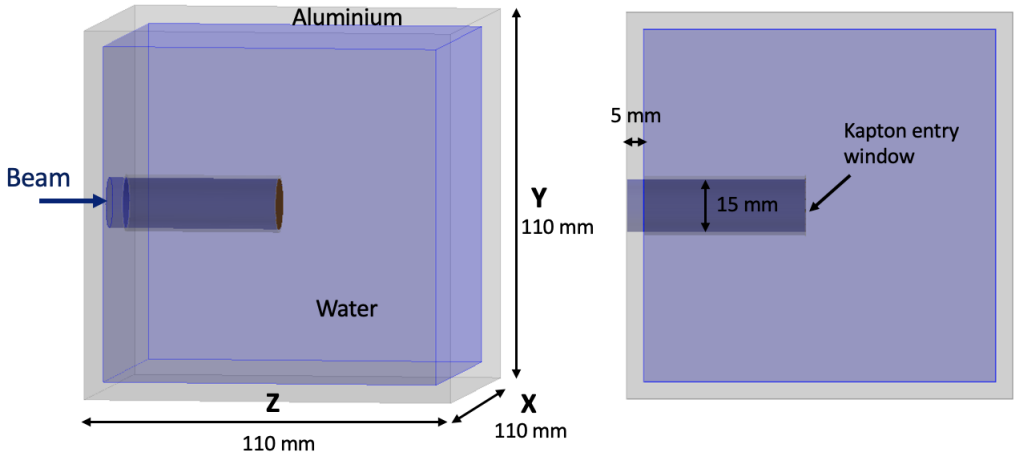

Figure 5. Geant4 simulation of the SmartPhantom. Angled view (left), cross-section view (right).

the source pressure distribution, caused by the incident beam, in the three orthogonal planes.

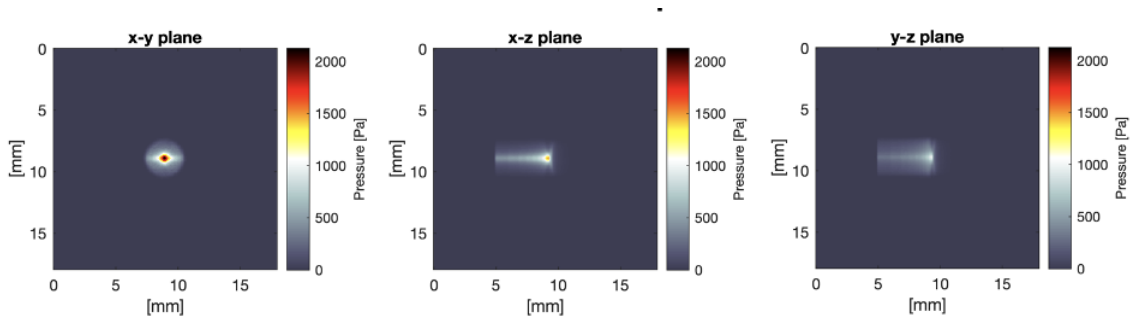

Figure 6. Source pressure distribution caused by the incident beam in the SmartPhantom.

4 Acoustic Signal

4.1 Generation & Propagation

The ion-acoustic pressure wave generation and evolution within the SmartPhantom have been simulated in k-Wave. Perfectly matched layer boundaries have been implemented in the simulation to prevent waves from being reflected at the boundaries.

4.2 Detection

The ion-induced pressure waves can be detected using acoustic transducers, such as piezoelectric sensors or ultrasonic detectors that can be placed within the medium [11]. Such transducers convert the pressure waves into electrical signals that can be further processed. Analyzing the time-of-flight and amplitude of these detected signals makes it possible to infer valuable information about the energy and dose distribution.

To initially showcase the simulation capabilities in dose-distribution reconstruction, the hemispherical sensor array shown in 7 was specified. Its location relative to the beam depositions is also illustrated.

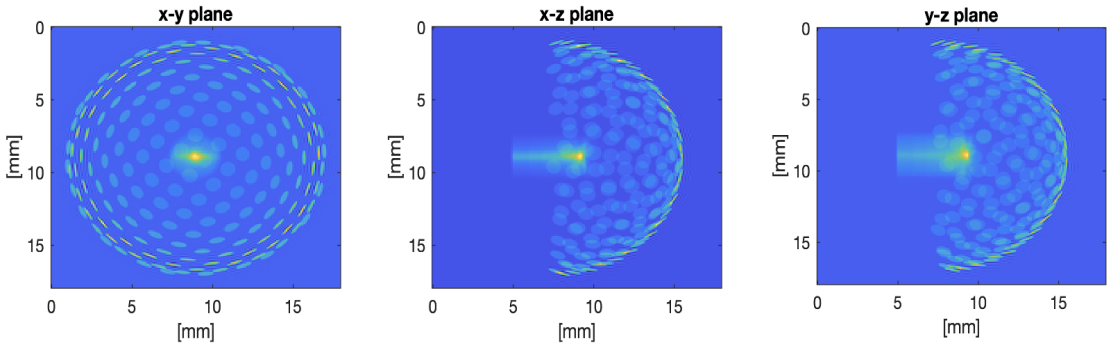

Figure 7. Simulated hemispherical sensor array and location. The sensor is made of 250 evenly distributed disk elements, 2 mm diameter each, and has a radius of 10 cm.

5 Image Reconstruction

Three image reconstruction methods to retrieve the 3D pressure profile have been investigated, with the best one being iterative time-reversal. To perform this reconstruction, the time-varying acoustic field generated by the source has been measured by the sensor. The measured signals at each element were propagated backwards in time and, subsequently, each element was treated as a point source. These emitted signals propagated back to the source where they interfered constructively and an image was formed [12]. The time-reversal method has been iterated to improve the estimate. The results are shown in Figure 8. From the results, it can be seen that the more iterations the better the result.

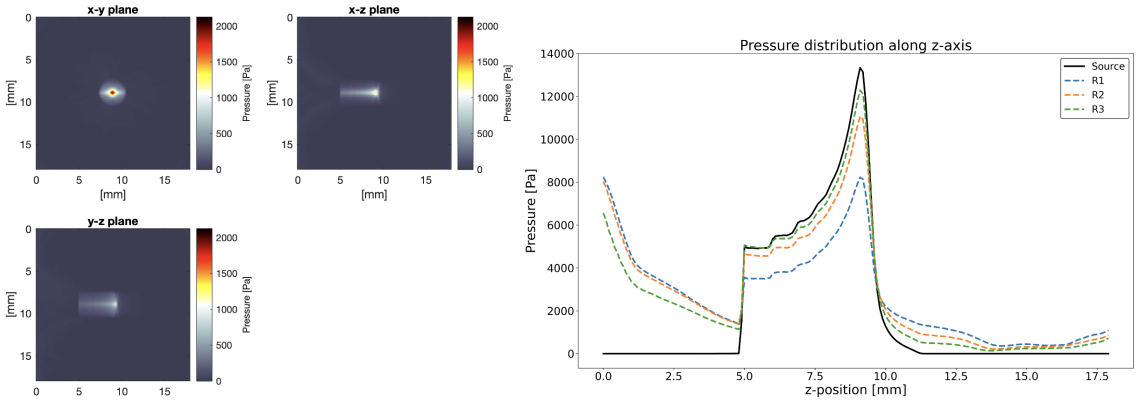

Figure 8. Reconstructed pressure distribution using an time-reversal algorithm. R1-3 corresponds to different iteration number.

6 Scintillating Fibre Plane Stations

Scintillating fibres are thin, flexible optical fibres [13]. They consist of a core material that produces scintillation when it interacts with high-energy particles and a cladding material that guides and protects the scintillation light within the fibre. The scintillation process involves the conversion of the absorbed energy into visible light and the emitted photons are then transmitted along the fibre by total internal reflection.

6.1 Design

A scintillating fibre plane consists of a series of scintillating fibres placed parallel to each other. To record radiation in two dimensions, two such planes can be placed perpendicularly to form a scintillating fibre detector or station. By employing multiple detectors positioned along the axis of the beam, the three-dimensional dose profile can be reconstructed by fitting an analytical approximation to the Bragg peak [14].

The scintillating fibre planes have been simulated, to enable the photon yield calculation, and subsequently, dose calculation at each depth. Due to the effective area of the beam, 20 x 20 mm square detectors have been modelled where each one is made of 66 fibres in each direction. Their location was chosen to be equidistant from each other and along the rising edge of the Bragg peak. A schematic diagram of the stations, as simulated in Geant4, is shown in Figure 9.

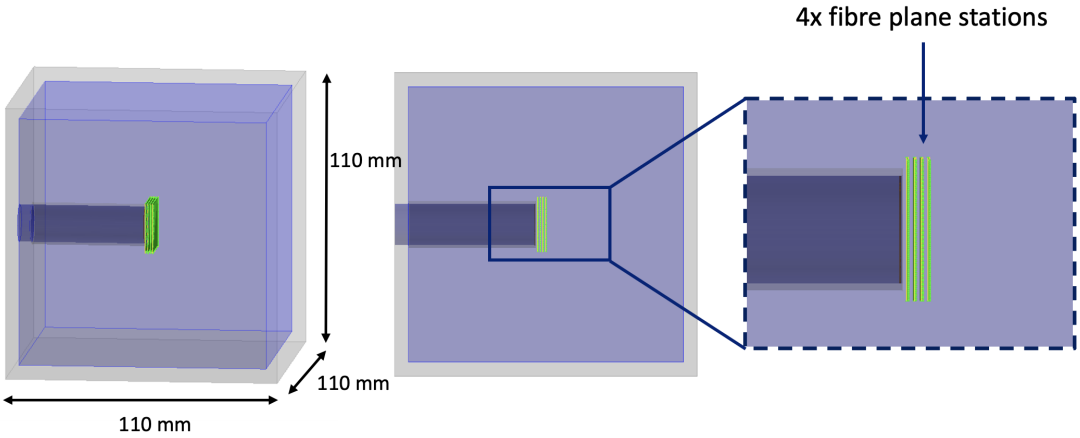

Figure 9. Geant4 simulation of the SmartPhantom with four scintillating fibre planes (green) placed equidistant from the end of the entrance window.

6.2 Reconstruction

The energy deposited in each single scintillating fibre has been used to reconstruct the 2D energy profile at each station. In an experiment, the energy in each fibre can be calculated based on the scintillating light detected and the photon yield of the material. The results of the reconstruction at each station are shown in Figure 10. From the results, it can be seen that the farther the station is from the entrance window, the larger the effective area of the beam depositions, which can be explained by Coulomb scatterings that occur as the beam propagates through the medium. From the results, it can also be seen that the closer the station is to the Bragg peak, the larger the energy depositions it detects, as expected.

7 Liquid Scintillator

Liquid scintillators can also be used for measuring the dose deposition profile [15]. When a high-energy ion beam passes through a liquid scintillator, it interacts with the scintillator molecules through various processes such as ionization, excitation, and nuclear reactions. These interactions can lead to the excitation of the scintillator molecules, and subsequently, cause the emission of scintillation light. Liquid scintillators have significant benefits such as forming a uniform solution and hence the attenuation of the acoustic signal is minimized. The scintillating light can be detected by a camera and the image analyzed to reconstruct the dose profile.

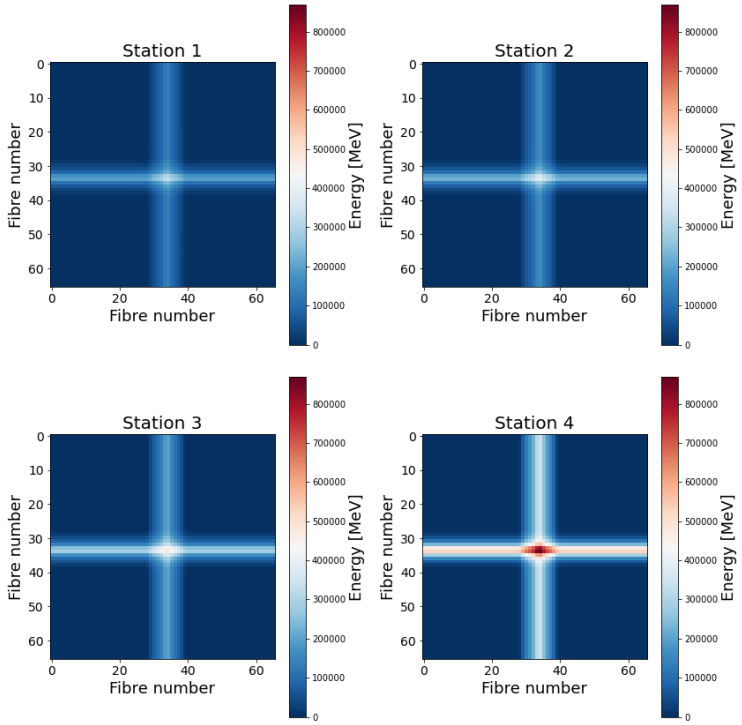

Figure 10. 2D reconstruction with the scintillating fibres' feedback at each station location. Station 1 is closer to the entrance window and Station 4 is closer to the Bragg peak.

7.1 Scintillating Solution

The Ultima Gold XR scintillating cocktail is planned to be used as the scintillating solvent, and be mixed with water [16]. The specific cocktail has been chosen as it has an undiluted density identical to water, which will ensure that the acoustic properties of the medium remain unchanged. To capture and focus the emitted scintillation light, a set of commercial bi-convex lenses and a CMOS camera are to be used.

7.2 Fluorescent Dye & UV Source

For a preliminary test of the intensity profile reconstruction using the proposed system, the fluorescent dye Coumarin-120 has been used to form a weak scintillating solution [17]. A commercially available UV LED has been used as the source and the UV light travelled through the solution enclosed in a BK7 glass water tank, followed by an air gap before the front surface of the imaging lens. An image was taken from a CMOS camera and analyzed in Python. The set-up was enclosed in a dark box to eliminate background light and is shown in Figure 11.

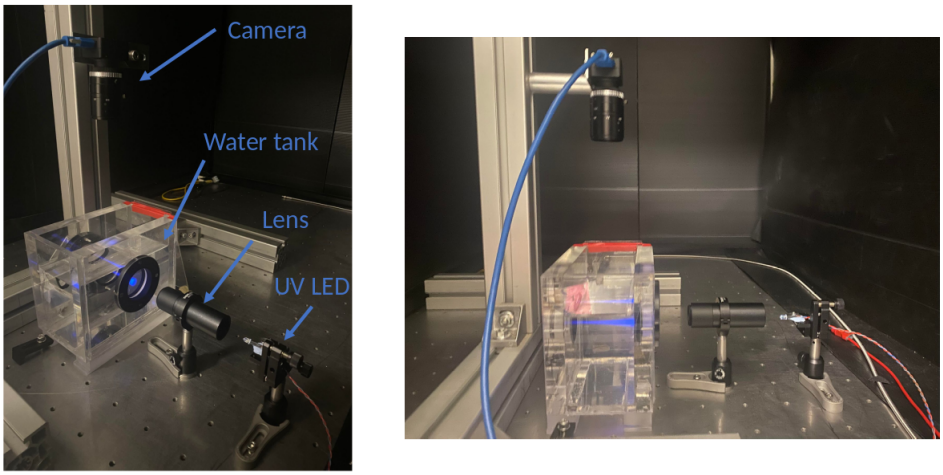

Figure 11. Fluorescent dye experimental set-up. Angled view (left), cross-sectional view (right).

Random noise was eliminated by taking 10 images of the background to form an average background image that was then subtracted from the captured image when the LED was powered on. The subtracted image, converted in grayscale, and the corresponding pixel intensity histogram are shown in Figure 12.

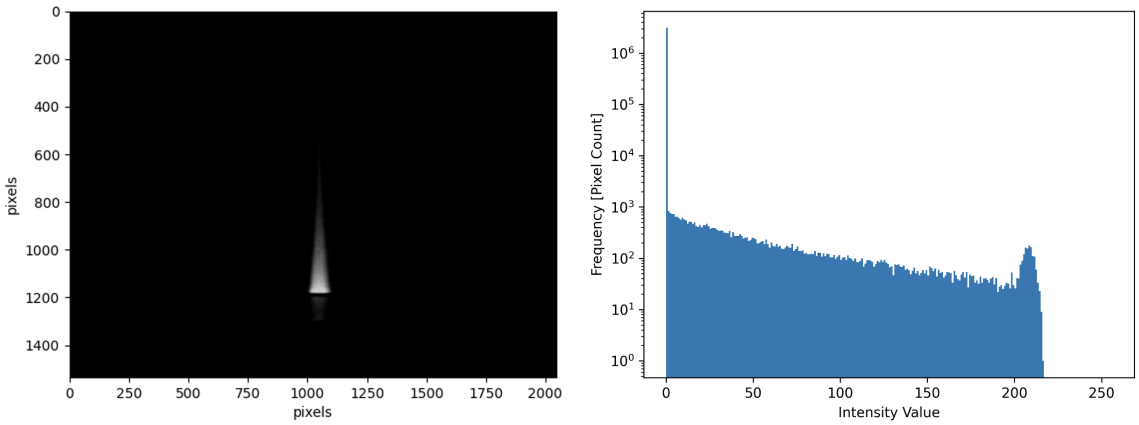

Figure 12. Captured image of the UV light travelling through the fluorescent solution, corrected for background noise and converted to grayscale (left) and histogram of the pixel intensities (right).

8 Discussion

LhARA is designed to revolutionize radiotherapy by delivering a flexibly controlled, patient-specific ion beam. Such a beam deposits most of its energy in a small volume of tissue at the

end of the particle's range. For this reason, a real-time dose-deposition mapping system is being developed to minimize radiation uncertainties. A proof-of-principle experiment, planned to be performed at the LION beamline facility, has been designed and simulated to evaluate the use of ionacoustic imaging in providing the dose-deposition profile. Scintillators have also been investigated to calibrate the acoustic response.

The BDSIM simulation of the LION beamline accurately modelled the incoming beam. The SmartPhantom simulated in Geant4 was also successful in providing the 3D energy depositions caused by the passage of the beam in water, and the pressure wave generation and propagation were successfully simulated with k-Wave. The specified acoustic sensor was also able to record the emitted acoustic signals which were then processed to reconstruct the dose profile. In addition, three different reconstruction methods were performed, with the iterative time-reversal reconstruction being the best one, as after only 3 iterations the reconstruction converged to the required result.

Scintillating fibres and liquid scintillators have also been proven to be a good solution to the 3D dose reconstruction by processing the scintillation light caused by the energy depositions of the beam. The data from the scintillating fibres were used to accurately reconstruct the 2D profile at various depths and a fluorescent dye solution experiment showed that it's feasible to reconstruct the intensity profile with a set of bi-convex lenses and a camera.

References

[1] Lehrer EJ, Prabhu AV, Sindhu KK, Lazarev S, Ruiz-Garcia H, Peterson JL, Beltran C, Furutani K, Schlesinger D, Sheehan JP, Trifiletti DM. Proton and Heavy Particle Intracranial Radiosurgery. Biomedicines. 2021 Jan 3;9(1):31. doi: 10.3390/biomedicines9010031. PMID: 33401613; PMCID: PMC7823941.

[2] Beard, P., 2011. Biomedical photoacoustic imaging. Interface Focus, 1(4), pp.602-631.

[3] www.sciencedirect.com. (n.d.). Scintillator - an overview | ScienceDirect Topics. [online] Available at: https://www.sciencedirect.com/topics/engineering/scintillator [Accessed 9 Oct. 2023].

[4] Python Software Foundation (2019). Welcome to Python.org. [online] Python.org. Available at: https://www.python.org.

[5] L.J. Nevay, S.T. Boogert, J. Snuverink, A. Abramov, L.C. Deacon, H. Garcia-Morales, H. Lefebvre, S.M. Gibson, R. Kwee-Hinzmann, W. Shields, S.D. Walker, BDSIM: An accelerator tracking code with particle–matter interactions, Computer Physics Communications, Volume 252, 2020, 107200, ISSN 0010-4655, https://doi.org/10.1016/j.cpc.2020.107200.

[6] CERN. 2020. User Documentation. [online] Available at: https://geant4.web.cern.ch/support/user_documentation. [Accessed 18 Apr. 2022].

[7] www.k-wave.org. (n.d.). k-Wave: A MATLAB toolbox for the time domain simulation of acoustic wave fields. [online] Available at: http://www.k-wave.org [Accessed 19 Mar. 2022].

[8] T. F. Rösch et al., "Laser-driven ION (LION) acceleration at the centre for advanced laser applications (CALA)," 2017 Conference on Lasers and Electro-Optics Europe & European Quantum Electronics Conference (CLEO/Europe-EQEC), Munich, Germany, 2017, pp. 1-1, doi: 10.1109/CLEOE-EQEC.2017.8087795.

[9] Fuchs, J., Antici, P., d'Humières, E. et al. Laser-driven proton scaling laws and new paths towards energy increase. Nature Phys 2, 48–54 (2006). https://doi.org/10.1038/nphys199

[10] Schreiber J, Bell F, Grüner F, Schramm U, Geissler M, Schnürer M, Ter-Avetisyan S, Hegelich BM, Cobble J, Brambrink E, Fuchs J, Audebert P, Habs D. Analytical model for ion acceleration by high-intensity laser pulses. Phys Rev Lett. 2006 Jul 28;97(4):045005. doi: 10.1103/PhysRevLett.97.045005. Epub 2006 Jul 28. PMID: 16907584.

[11] Easy Tech Junkie. (2023). What is an Acoustic Transducer? (with pictures). [online] Available at: https://www.easytechjunkie.com/what-is-an-acoustic-transducer.htm [Accessed 9 Oct. 2023].

[12] Huang, Chao et al. "Full-wave iterative image reconstruction in photoacoustic tomography with acoustically inhomogeneous media." IEEE transactions on medical imaging vol. 32,6 (2013): 1097-110. doi:10.1109/TMI.2013.2254496

[13] D. Lo Presti, G. Gallo, D. Luigi Bonanno, D. Giuseppe Bongiovanni, F. Longhitano, and S. Reito, Real-Time Particle Radiography by Means of Scintillating Fibers Tracker and Residual Range Detectors. IntechOpen, Apr 2019. [Online]. Available: http://dx.doi.org/10.5772/intechopen.81784

[14] Bortfeld T. An analytical approximation of the Bragg curve for therapeutic proton beams. Med Phys. 1997 Dec;24(12):2024-33. doi: 10.1118/1.598116. PMID: 9434986.

[15] Callaghan, E.J., Goldblum, B.L., Brown, J.A. et al. Measurement of proton light yield of water-based liquid scintillator. Eur. Phys. J. C 83, 134 (2023). https://doi.org/10.1140/epjc/s10052-023-11242-2

[16] Elmer, P. (2020). Safety data sheet. [online] Available at: https://resources.perkinelmer.com/corporate/content/msdsdatabase/msd_6013119_ultima_gold_xr_(gb).pdf [Accessed 15 Sep. 2023].

[17] Can Wang et al 2021 Laser Phys. 31 025801 DOI 10.1088/1555-6611/abd565